Appl Phys B (2009) 97: 387–396
DOI 10.1007/s00340-009-3736-0

Applied Physics B
Lasers and Optics

Bragg spectroscopy and Ramsey interferometry with an ultracold Fermi gas

B. Deh · C. Marzok · S. Slama · C. Zimmermann · P.W. Courteille

Received: 4 February 2009 / Revised version: 12 August 2009 / Published online: 17 September 2009

Abstract We report on the observation of Bragg scattering of an ultracold Fermi gas of ^{6}Li atoms at a dynamic optical potential. The momentum states produced in this way oscillate in the trap for time scales on the order of seconds, nearly unperturbed by collisions, which are absent for ultracold fermions due to the Pauli principle. In contrast, interactions in a mixture with ^{87}Rb atoms lead to rapid damping. The coherence of these states is demonstrated by Ramsey-type matter wave interferometry. The signal is improved using an echo pulse sequence, allowing us to observe coherence times longer than 100 μs. Finally, we use Bragg spectroscopy to measure the in-situ momentum distribution of the ^{6}Li cloud. Signatures for the degeneracy of the Fermi gas can be observed directly from the momentum distribution of the atoms inside the trap.

PACS 67.85.Pq · 37.25.+k · 03.75.Ss

1 Introduction

Bragg diffraction of cold atoms at propagating standing light waves is used in two distinct ways, as Bragg spectroscopy to measure the momentum distribution of ultracold gases [1, 2] and as beamsplitter for coherent atom optics [3]. Bragg spectroscopy has developed into a powerful tool for measuring the dispersion relation and the dynamic structure factor of cold gases. It was used to observe the momentum distribution of trapped Bose–Einstein condensates (BEC) [1, 2, 4–7], the structure factor of molecular condensates [8] and to study signatures of vortices [9, 10]. Furthermore, the technique is discussed for measuring the dynamic structure factor in the presence of long-range particle correlations, such as superfluid pairing in a Fermi gas or fermionic condensation [11–13].

Because Bragg diffraction coherently couples two momentum states, it is frequently used as a beamsplitter for matter waves in interferometric experiments [14]. A BEC seems the optimal candidate for such an interferometer, because the macroscopically populated wavefunction yields a high interferometric contrast. Consequently, a number of interferometric experiments have been done using Bragg diffraction of a BEC, e.g. [15, 16]. However, in the case of a BEC, the two momentum states resulting from the Bragg diffraction interact with each other via s-wave collisions [17, 18]. This interaction is prominently observed in time-of-flight (TOF) absorption images as a halo forming between the diffraction peaks. The typical lifetime of coherent superposition states due to interatomic interactions therefore is limited to only a few tens of microseconds [19]. Such experiments are thus performed during TOF or in very weak traps.

Superposition states in a Fermi gas, however, can live for a very long time as has been observed for potassium atoms in an optical lattice [20]. Since fermions do not interfere, the matter wave contrast is necessarily limited to single-particle interference, but the long coherence lifetime nevertheless

B. Deh (✉) · C. Marzok · S. Slama · C. Zimmermann · P.W. Courteille
Physikalisches Institut, Eberhard-Karls-Universität Tübingen, Auf der Morgenstelle 14, 72076 Tübingen, Germany
e-mail: deh@phas.ubc.ca
Fax: +1-604-8225324

B. Deh
Department of Physics and Astronomy, University of British Columbia, 6224 Agricultural Road, Vancouver, B.C., V6T 1Z1, Canada

makes fermions excellent candidates for interferometric experiments.

In this paper we report on Bragg diffraction of ultracold fermions from a light grating realized by two slightly detuned counterpropagating laser beams. The diffraction was analyzed by studying Rabi oscillations between the two coupled momentum states for low intensities of the Bragg lasers. Increasing the intensity of the Bragg light eventually leads to Kapitza–Dirac scattering. We also studied the transition between Bragg and Kapitza–Dirac scattering. Here, the system is no longer well described as a two-level system, and a multilevel ansatz has to be used. Experimental results of scattering in the Kapitza–Dirac regime and their theoretical description are presented.

Furthermore, we used Bragg spectroscopy to map the momentum distribution of the ^{6}Li cloud. As there is no interaction between identical fermions in the ultracold regime, the momentum distribution directly reflects the thermal distribution given by the Fermi–Dirac statistics. With a temperature of $T/T_\mathrm{F} = 0.6$ the onset of degeneracy can be found by comparing Maxwell–Boltzmann and Fermi–Dirac fits to the measured momentum distribution [21].

The diffracted momentum states oscillate in the trap for several seconds nearly unperturbed, which is only possible because of suppression of s-wave collisions due to the Pauli principle. Higher partial waves are frozen out at the ultralow temperatures realized in the experiment. In particular, p-wave collisions are suppressed at temperatures below approximately 100 μK [22]. The oscillation is eventually destroyed by dephasing due to the anharmonicity of the trap. Furthermore, the lifetime of oscillating atoms is dramatically reduced in the presence of ^{87}Rb atoms that collide with the ^{6}Li atoms.

We also report on Ramsey interferometry with ultracold fermions, based on Bragg diffraction of trapped ^{6}Li atoms. A complete Ramsey spectrum can be taken in a single experimental cycle and is recorded by absorption imaging after TOF. We observe Ramsey fringes for holding times of more than 30 μs. For longer times, the fringes cannot be resolved by the imaging system.

The limitation can be overcome by echo techniques similar as in NMR [23]. This method has already been applied in atomic beam experiments [14] as well as in interferometric experiments with BECs [16]. In our experiment a diffraction echo is generated by a two-photon Bragg pulse located halfway in time between the Ramsey pulses. Hence, we realize a motional wavepacket echo by optical means in a similar way as is done in a Ramsey–Bordé interferometer [24]. Our paper extends previous work presented in [25].

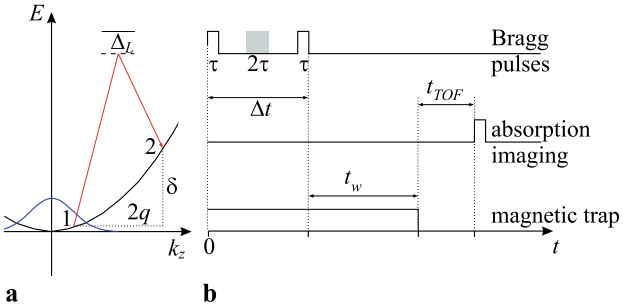

Fig. 1 Schematics of a Bragg diffraction experiment. (**a**) Dispersion parabola of (quasi-) free particles. Shown is the initial Gaussian momentum distribution of the atoms and the Bragg transition between the initial state 1 and the final state 2 with a momentum shift of $2\hbar q$. (**b**) Typical pulse sequence of a Bragg diffraction experiment. For single-pulse experiments only the first Bragg pulse is applied. For a Ramsey experiment two $\pi/2$ pulses are used. For a diffraction echo experiment, a third pulse (*shaded area*) is centered between the Ramsey pulses

2 Experimental procedure

To achieve simultaneous quantum degeneracy of ^{6}Li and ^{87}Rb, we use a procedure detailed in previous papers [25, 26]. ^{6}Li atoms provided by a Zeeman slower and ^{87}Rb atoms ejected from dispensers [27] are simultaneously collected by a magneto-optical trap. They are subsequently transferred via several intermediate magnetic traps into a Ioffe–Pritchard-type trap, where they are stored in their respective hyperfine states $|F, m_F\rangle = |3/2, 3/2\rangle$ and $|2, 2\rangle$. The secular frequencies of this (compressed) trap are $(\omega_x, \omega_y, \omega_z)/2\pi = (762, 762, 190)$ Hz for ^{6}Li and the magnetic field offset 3.5 G. For ^{87}Rb the trap frequencies are $\sqrt{87/6}$ times lower. The ^{87}Rb cloud is selectively cooled by microwave-induced forced evaporation and serves as a cooling agent for the ^{6}Li cloud, which adjusts its temperature to the ^{87}Rb cloud through interspecies thermalization. However, due to the small interspecies scattering length, $a = -20a_B$ [26, 28], the thermalization is slow. Therefore, at low temperatures, when the size of the evaporated ^{87}Rb cloud becomes small or in shallow traps, where the different gravitational sag separates the two species, the clouds thermally decouple. For the experiments described below, we typically reach temperatures of below 1 μK with 2.5×10^6 ^{87}Rb atoms and 1.5 μK with 2×10^5 ^{6}Li atoms. The respective densities are 2×10^{13} cm^{-3} for ^{87}Rb and 4×10^{12} cm^{-3} for ^{6}Li, which corresponds to the critical temperature $T_c = 0.7$ μK and the Fermi temperature $T_\mathrm{F} = 2.4$ μK.

For most experiments (unless stated otherwise) we use a decompressed magnetic trap with trap frequencies $(\omega_x, \omega_y, \omega_z)/2\pi = (236, 180, 141)$ Hz. Decompression lowers the temperatures of the clouds, but increases their gravitational sags. ^{6}Li is much lighter than ^{87}Rb, so that the two clouds separate in space, and the ^{6}Li cloud thermally

decouples from the ^{87}Rb cloud. Since ^{6}Li cannot thermalize by itself, the adiabatic cooling upon decompression becomes anisotropic. The temperature measured along the z-axis, along which the Bragg diffraction is performed, is then $T_z \simeq 0.9$ μK.

2.1 Bragg diffraction

The ^{6}Li atoms are Bragg-diffracted by means of two counterpropagating laser beams aligned along the z-axis of the Ioffe–Pritchard trap. The laser beams are frequency-shifted by acousto-optic modulators (AOM). One AOM is driven by a stable quartz oscillator at 100 MHz. The other AOM is driven by a voltage-controlled oscillator, which is phase-locked to the quartz oscillator by means of an electronic feedback loop. The frequencies of the two laser beams (ω_1 and ω_2) are set to differ by an amount $\delta = \omega_2 - \omega_1$ which, in most cases, is equal to the two-photon recoil shift $2\hbar q^2/m = 2\pi \times 295$ kHz, with $q = 2\pi/\lambda$ and λ is the resonant wavelength of the D_2 line of ^{6}Li. The Bragg beams have intensities of $I_1 = I_2 = 13.7 \ldots 132$ mW/cm^2. The laser frequencies are tuned $\Delta_L/2\pi \simeq 1$ GHz red to the D_2 line, so that the two-photon Rabi frequency reaches values between $\Omega_\mathrm{R} = 3\pi c^2 \Gamma I/\hbar\omega^3 \Delta_L \simeq 2\pi \times 47 \ldots 450$ kHz. The pulse duration is chosen to generate specific pulse areas $\Phi = \Omega_\mathrm{R}\tau/2\pi$. In most experiments, before applying the Bragg pulse, the ^{87}Rb atoms are removed from the trap by means of a resonant light pulse. After the Bragg pulse we wait for a time t_w before switching off the trapping field and recording absorption images revealing the momentum distribution of the ^{87}Rb and ^{6}Li clouds. In some (Ramsey) experiments, we apply a second Bragg pulse separated from the first one by a time interval Δt, or even a third one at half time between the two others (see Fig. 1).

2.2 Imaging

Figure 2(a–d) show typical ^{6}Li absorption images taken after application of a Bragg pulse. For this, the atoms are held in the trap for a short time (3–4 ms depending on the trap geometry) then the atoms are released from the trap and expand freely for 0.8–1.1 ms. After this the atoms are illuminated with resonant light and their shadow is recorded on a CCD camera. The waiting time in the trap and the time for ballistic expansion are chosen, such that the images reflect the momentum distribution of the atoms right after the Bragg pulse and are well resolved, while still having a good signal to noise ratio.

The effect of the Bragg pulse on the atoms can therefore be read directly from these images. For low intensity of the Bragg beams, only a narrow slice is cut out of the fermionic momentum distribution. The position of the slice along the z-axis depends on the detuning $\Delta = 2\hbar q^2/m - \delta$ of the Bragg lasers from the two-photon recoil shift. The width is due to power broadening by the Rabi frequency Ω_R.

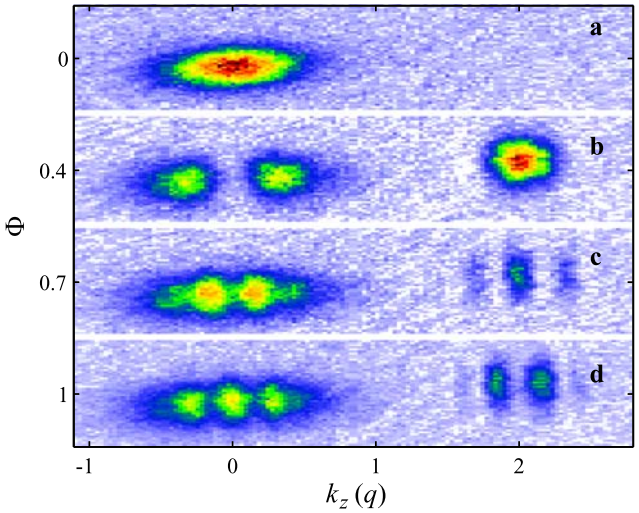

Fig. 2 TOF absorption images taken after a Bragg scattering pulse followed by a 4 ms waiting time (half a trap period for rephasing) and a 2 ms ballistic expansion. From (**a**) to (**d**) the Bragg pulse duration is varied such that the pulse area is $\Phi = \Omega_\mathrm{R}\tau/2\pi = 0, 0.4, 0.7, 1$

3 Theoretical model

3.1 Free particles

We describe our experimental observations with the following model [29]. We assume that during a Bragg pulse only two discrete momentum states $j = 0, 1$ of an atom are coupled and that the impact of the trapping potential can be neglected. This is justified for sequences much shorter than the trap oscillation period, i.e. $\tau, \Delta t \ll 2\pi/\omega_z$. The probability amplitudes of the two states are denoted by a_{j,k_z}. They correspond to atoms with initial momentum $\hbar k_z$ that are coupled to states with momentum $\hbar k_z' = \hbar(k_z + 2q)$. The time evolution of the amplitudes under the action of the Bragg light is given by the solution of the Schrödinger equation

$$\begin{pmatrix} a_{0,k_z}(t) \\ a_{1,k_z}(t) \end{pmatrix} = e^{-iH_\tau t/\hbar} \begin{pmatrix} a_{0,k_z}(0) \\ a_{1,k_z}(0) \end{pmatrix}, \tag{1}$$

with the Hamiltonian

$$H_\tau = \begin{pmatrix} \frac{\hbar}{2m}k_z^2 & \frac{1}{2}\Omega_\mathrm{R} \\ \frac{1}{2}\Omega_\mathrm{R} & \frac{\hbar}{2m}k_z'^2 - \delta \end{pmatrix}. \tag{2}$$

When the Bragg light is turned off, the Hamiltonian simplifies to

$$H_{\Delta t} = \begin{pmatrix} \frac{\hbar}{2m}k_z^2 & 0 \\ 0 & \frac{\hbar}{2m}k_z'^2 - \delta \end{pmatrix}. \tag{3}$$

By concatenating time evolutions described by $e^{-iH_\tau t/\hbar}$ and $e^{-iH_{\Delta t} t/\hbar}$, the phase evolution of individual atoms in a superposition of momentum states can be calculated for arbitrary sequences of pulses separated by times of free evolution, e.g. Ramsey-type sequences.

Initially the atoms are inhomogeneously distributed in momentum space. This distribution is governed by Fermi–Dirac statistics. In the temperature range of our experiments ($T/T_F \geq 0.6$) however, the distribution does not deviate much from Maxwell–Boltzmann statistics, such that the momentum distribution can be assumed as

$$\phi(k_z) = \hbar/\left(2\pi m k_B T\right)^{1/2} e^{-\hbar^2 k_z^2/2mk_B T}. \tag{4}$$

To obtain the momentum distribution of the atoms after an applied pulse sequence, we calculate the evolution of the amplitudes a_{j,k_z} for a variety of initial momenta and weight the final populations of the momentum states with the distribution function $\phi(k_z)$. The number of atoms in the zeroth- and first-order Bragg-diffracted modes is then

$$N_j(t) = \int \phi(k_z)\left|a_{j,k_z}(t)\right|^2 dk_z. \tag{5}$$

The procedure neglects atomic interactions, which certainly is a good assumption for an ultracold Fermi gas [22].

3.2 Trapped particles

If trapped atoms are considered, the problem arises that the momentum eigenstates are simultaneously coupled by two interactions, the moving optical lattice and the harmonic trap. However, the situation is simplified, if a separation of scales is possible. In general, the duration of a pulse is very short, $\tau \ll 2\pi/\omega_z$. In contrast, the duration of a waiting time period Δt can be such that it is no more negligible compared to a trap oscillation period. For these time intervals, the action of the trapping potential must explicitly be taken into account.

Because the trap couples the atomic momenta and positions, the initial spatial distribution of the atoms must now be considered. For simplicity we describe it as a thermal Gaussian function, similar as done in (4) for the momentum distribution,

$$\psi(z) = \left(m\omega_z^2/2\pi k_B T\right)^{1/2} e^{-m\omega_z^2 z^2/2k_B T}. \tag{6}$$

Starting from initial positions z and momenta k_z, a diffraction pulse transfers the recoil $2q$ to a part of the atoms. If the pulse length is short enough, the atomic position is not altered. The atoms then follow the classical trajectories

$$\begin{aligned} \tilde{k}_z(t) &= k_z \cos\omega_z t - \frac{\hbar\omega_z}{m} z \sin\omega_z t, \\ \tilde{k}'_z(t) &= (k_z + 2q)\cos\omega_z t - \frac{\hbar\omega_z}{m} z \sin\omega_z t, \end{aligned} \tag{7}$$

where the first expression holds for undiffracted atoms and the second for diffracted atoms. These values are used instead of k_z and k'_z respectively, in the Hamiltonians (2) and (3). As the Bragg pulses are short compared to the oscillation period, $\tau \ll 2\pi/\omega_z$, the effect of the trapping potential can be neglected for the description of the Bragg diffraction. This means that the Hamiltonian H_τ depends on $\tilde{k}_z(t)$, but can be treated as time-independent during the short time intervals τ. In contrast, the free propagation Hamiltonian $H_{\Delta t}$ gets time-dependent if Δt is long. In this case, the phase evolution of the atoms in both coupled momentum states can be described by writing the time-evolution operator as

$$e^{-\frac{i}{\hbar}H_{\Delta t}t} = \begin{pmatrix} e^{\left(-i\int_0^t dt\,\frac{\hbar}{2m}\tilde{k}_z^2(t)\right)} & 0 \\ 0 & e^{\left(-i\int_0^t dt\left[\frac{\hbar}{2m}\tilde{k}_z'^2(t)-\delta\right]\right)} \end{pmatrix}. \tag{8}$$

Since the amplitudes a_{j,z,k_z} now also depend on the initial atomic positions, the final populations of the momentum states must additionally be weighted by the initial spatial distribution. Therefore, (5) for the expectation values of the diffracted and non-diffracted atom numbers now reads

$$N_j(t) = \iint \phi(k_z)\psi(z)\left|a_{j,z,k_z}(t)\right|^2 dk_z\, dz. \tag{9}$$

4 Single pulse experiments

4.1 Bragg diffraction

We first study diffraction with a single Bragg pulse. Having applied a pulse of a given length, we observe an axial modulation of the momentum distribution. This is due to the fact that different velocity classes of the atomic clouds have different Doppler shifts with respect to the Bragg lasers and therefore are subject to different Rabi flopping frequencies. The initial momentum distribution thus leads to an inhomogeneous population of the two momentum states after the pulse.

For small pulse areas Φ only momenta around $\hbar k_z = 0$ are diffracted. With increasing Φ nonresonant velocity classes are also coupled by the Bragg beams as can be seen in Figs. 3(a) and (c). The interpretation is supported by a theoretical simulation shown in Figs. 3(b) and (d), which has been done by computing the evolution of the momentum distribution according to (2) and (4). Note, that the width of the initial momentum distribution exceeds the power and Fourier broadening in this experiment.

The total amount of undiffracted and diffracted atoms is obtained by integration of the momentum distributions in the zeroth- and first-order Bragg-diffracted clouds, respectively. The measured difference between the number of atoms in the first and zeroth order normalized to the total atom number is shown in Fig. 4 (crosses) as a function of pulse duration. The observed damped Rabi oscillations are reproduced by theory doing the same integration for the simulated

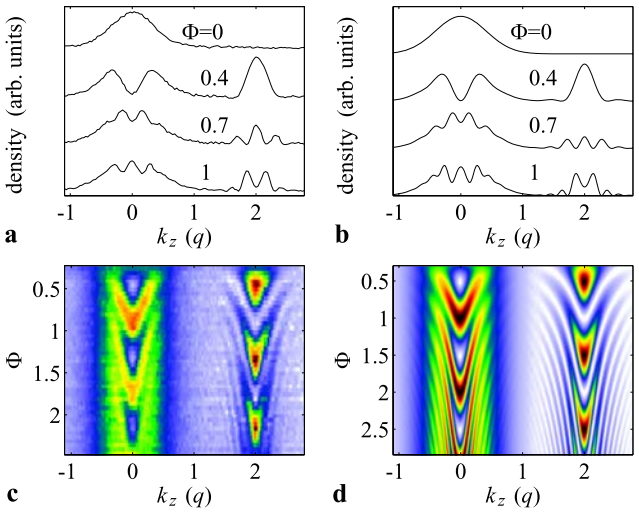

Fig. 3 (**a**) Integration of the TOF absorption images shown in Fig. 2 along the radial direction (perpendicular to **q**). (**b**) Simulation of the axial momentum distribution after a Bragg pulse with same pulse area as in (**a**). (**c**) False color map of measured momentum distributions with pulse areas ranging between $\Phi = \Omega_R \tau/2\pi = 0 \ldots 2.8$. The radially integrated absorption images appear as rows. (**d**) Calculation of the false color map with the experimental parameters used for the measurement (**c**)

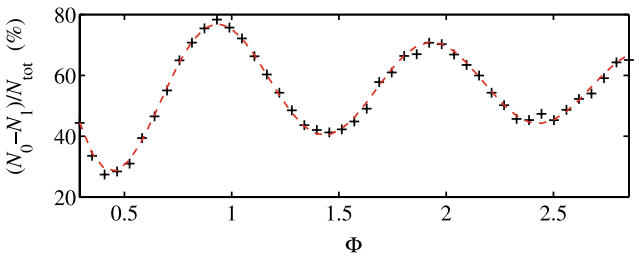

Fig. 4 Difference between the measured number of atoms in the zeroth- and first-order Bragg-diffracted clouds for variable duration of the Bragg pulse. The (*black*) *dots* are the experimental data, the (*red*) *dashed line* is a theoretical simulation according to (5)

momentum distribution according to (5), as can be seen in Fig. 4 as a (red) dashed line. Note that the damping is solely due to the initial inhomogeneous momentum distribution, decoherence was not included in the simulations.

4.2 Kapitza–Dirac scattering

For larger Rabi frequencies,

$$\Omega_R \gg \frac{2\hbar q \sigma_{k_z}}{m}, \tag{10}$$

with $\sigma_{k_z} = \sqrt{m k_B T/\hbar^2}$ being the width of the momentum distribution, the Doppler broadening is dominated by power broadening, meaning that all atoms can be diffracted into the first order simultaneously.

At some point, however, the Rabi frequency becomes comparable to the energy difference between adjacent momentum states, and Kapitza–Dirac scattering sets in. According to [29] the scattering will stay two-state-like as long as the Rabi frequency fulfills the condition

$$\Omega_R \ll \frac{\hbar}{m}\left(4q^2 - 2q\sigma_{k_z}\right). \tag{11}$$

In the Kapitza–Dirac regime, the large energy uncertainty, connected with the fast coupling rate, allows several momentum states to be coupled simultaneously. The resulting dynamics can be described by a simple extension of the model detailed in Sect. 3. In particular the Hamiltonian (2) is replaced by

$$H_\tau = \begin{pmatrix} \ddots & \ddots & & & \\ \ddots & \frac{\hbar(k_z-2q)^2}{2m} + \delta & \frac{\Omega_R}{2} & & \\ & \frac{\Omega_R}{2} & \frac{\hbar k_z^2}{2m} & \frac{\Omega_R}{2} & \\ & & \frac{\Omega_R}{2} & \frac{\hbar(k_z+2q)^2}{2m} - \delta & \ddots \\ & & & \ddots & \ddots \end{pmatrix}. \tag{12}$$

The crossover from the Bragg diffraction regime towards Kapitza–Dirac scattering is a smooth transition. As we will see below, for intermediate Rabi frequencies (here 1 MHz > $\Omega_R/2\pi$ > 100 kHz) the neighboring diffraction states, corresponding to momentum shifts of $4\hbar q$ and $-2\hbar q$ (second and minus first order), are scarcely populated. For increasingly higher Rabi frequencies, $\Omega_R/2\pi > 1$ MHz, the scattering populates more and more diffraction orders.

We performed Bragg diffraction at the transition between the Bragg and Kapitza–Dirac regime by increasing the Bragg laser intensity beyond the value used in the experiments discussed in the previous sections. Figure 5(a) shows the atomic distribution as a function of Φ after 2 ms TOF for such an experiment. A simulation using (12) is shown in Fig. 5(b). This simulation reproduces the experimental results very well and reveals a Rabi frequency of $\Omega_R = 2\pi \times 420$ kHz.

In some cases it is desirable to diffract all atoms simultaneously into the first order. This is only feasible by combining the Bragg regime (11), $\Omega_R \ll \frac{\hbar}{m}(4q^2 - 2q\sigma_{k_z})$ with large power broadening (10), $\Omega_R \gg 2\hbar q\sigma_{k_z}/m$. The resulting condition,

$$k_B T \ll \frac{\hbar^2 q^2}{m}, \tag{13}$$

is satisfied for temperatures $T \ll 7$ μK. The temperature reached in this experiment is within this regime.

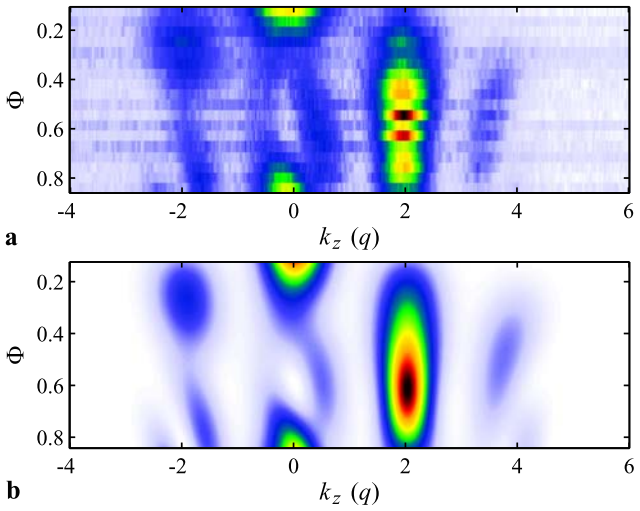

Fig. 5 (**a**) False color map of measured momentum distributions similar to Fig. 3. The Rabi frequency was chosen such that the system is approaching the Kapitza–Dirac regime. While the main diffraction is between the momentum states of $0\hbar q$ and $2\hbar q$ (zeroth- and first-order diffraction states), diffraction into the $-2\hbar q$ and $4\hbar q$ states also occur. The pulse area was changed by applying different pulse lengths. (**b**) Theoretical simulation of the momentum distribution in (**a**) using (12). The Rabi frequency chosen for the simulation was $\Omega_R = 2\pi \times 420$ kHz

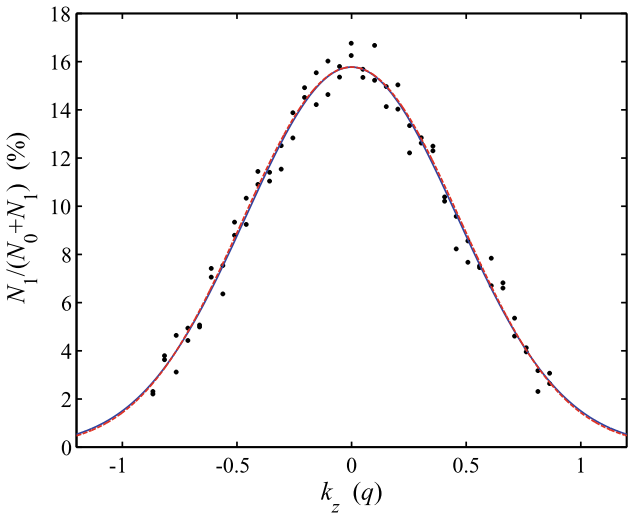

Fig. 6 Momentum distribution of the trapped ^{6}Li cloud measured by Bragg spectroscopy. The *blue* (*solid*) *line* is a Gaussian fit to the data, revealing a temperature of 1.5 μK. The *red* (*dashed*) *line* is a simulated Fermi–Dirac momentum distribution for 2×10^5 atoms at 1.4 μK. These two curves are nearly indistinguishable in the plot

4.3 Bragg spectroscopy

For a given frequency detuning δ the Bragg lasers address a specific momentum class $\hbar k_z$ of the atomic cloud [1, 2],

$$\delta = \frac{2\hbar q^2}{m} + \frac{2\hbar q k_z}{m}. \tag{14}$$

This implies a linear dependence between detuning and addressed momentum class. It is thus possible to probe the momentum distribution by measuring the number of Bragg-diffracted atoms as a function of the detuning.

Figure 6 shows a spectrum resulting from such a series of measurements, performed in the compressed trap. In this experiment, the pulse duration was chosen such that the pulse area was $\Phi \simeq 0.5$. The frequency detuning of the two Bragg lasers was changed between 40 kHz and 550 kHz in 15 kHz steps, which is small compared to the Rabi frequency $\Omega_R \simeq 2\pi \times 58$ kHz. In Fig. 6 the amount of scattered atoms is plotted versus the resonant atomic momentum derived from (14). The data show a distinctive Gaussian shape, corresponding to the temperature $T = 1.50\ \mu\text{K} \pm 0.15\ \mu\text{K}$ (blue, solid curve), in good agreement with TOF measurements.

At low temperatures $T \ll T_F$, the momentum distribution is expected to deviate from a Gaussian profile and to adopt the shape of an inverted parabola. However, in our experiments the temperatures were not far below the Fermi temperature of $T_F \simeq 2.4$ μK. In this regime, the distributions, integrated in the two dimensions perpendicular to the z-axis, have quite similar shapes. A fit based on a Fermi–Dirac distribution for 1.8×10^5 atoms is also shown in Fig. 6 as red (dashed) curve. This fit yields a temperature of $T = 1.39\ \mu\text{K} \pm 0.18\ \mu\text{K}$.

The two curves, for the Gaussian and the Fermi–Dirac distribution are nearly congruent. Although the shape of the momentum distribution thus provides no clear signal for degeneracy in this regime, the result suggests that the temperatures due to Gaussian fits are overestimated by 5 . . . 10%.

Bragg spectroscopy yields the same information as standard TOF absorption imaging. However, this technique reveals the momentum distribution inside the trap. Adiabatic cooling and magnetic field distortions during trap switch-off do not affect the signal, which is particularly important for light and fast atoms such as lithium.

4.4 Trap dynamics

By Bragg diffraction the atoms acquire additional momentum and begin to oscillate inside the trap. This oscillation has been analyzed in the following experiment. A fraction of the atoms, stored in the compressed trap, is Bragg-scattered by a single π-pulse. The atoms are then held inside the trap for variable holding times t_w before being imaged (see Fig. 7).

Several observations are made: If no ^{87}Rb is in the trap, the ^{6}Li atoms oscillate for times on the order of seconds; however, the distribution of the diffracted atoms smears out. Also, the oscillation period of the diffracted atoms differs from the period of undiffracted atoms. The momentum distribution of these undiffracted atoms is depleted around

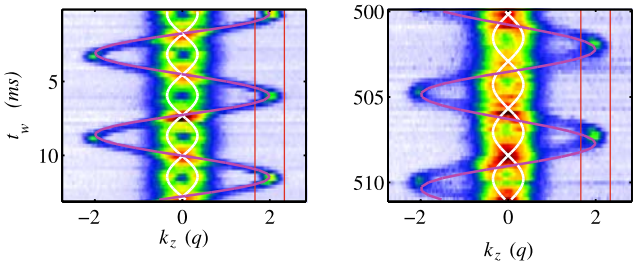

Fig. 7 Momentum distribution after a π-pulse and a variable waiting time t_w in the trap. Diffracted and undiffracted atoms oscillate in a potential given in good approximation by (15). The equation of motion for this oscillation has been computed and is shown as (*white* and *magenta*) *curves*. The oscillation period for the two amplitudes differ, as can be seen for large waiting times $t_w \gg 2\pi/\omega_z$. The (*red*) *lines* indicate the area in which the atom numbers were counted for analysis in Fig. 8

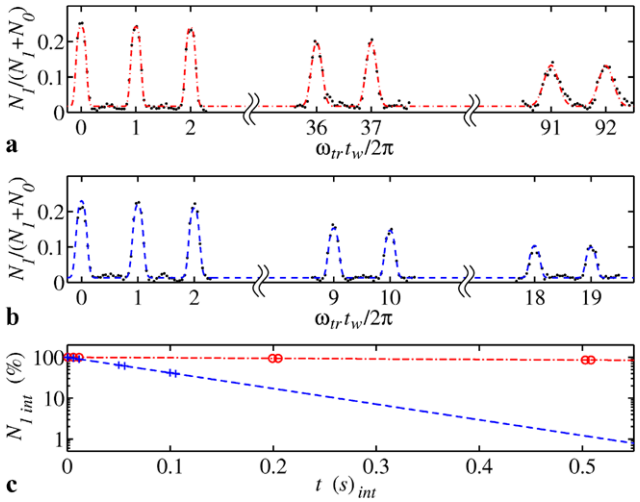

Fig. 8 Rephasing of the momentum distribution in the trap in the absence (**a**) and in the presence (**b**) of ^{87}Rb. Plotted are the integrated numbers of Bragg-diffracted atoms found at a given time t_w after an initial Bragg π-pulse in a restricted area of the momentum space. The fit is a combination of an error function with linearly increasing Gaussian width and an exponential damping of the peak height. This damping is best observed in (**c**), where the integrated number of atoms in each peak is plotted versus time in a logarithmic plot. Only small damping is observed in the absence of ^{87}Rb (*black*, *dash-dotted curve*), while the presence of ^{87}Rb induces a fast damping (*red*, *dashed curve*)

$k_z = 0$, because atoms in low momentum states are Bragg-scattered preferentially. Atoms in the zeroth order oscillate with an average amplitude given by the width of the thermal distribution of the original cloud, as can be seen in Fig. 7.

The broadening of the momentum distribution as well as the different oscillation periods for the two diffraction orders are due to anharmonicities in the magnetic trap. The magnetic potential of the trap is a combination of the quadrupole field generated by a pair of coils in anti-Helmholtz configuration and the field generated by four wires parallel to the rotational axes of the coils. The numerically calculated field geometry is in very good approximation given by [30]

$$B_z(z) = B_0 - \alpha(z+a) + \beta a^2 e^{z/a}, \tag{15}$$

with the gradient α, the curvature β and $a = \alpha/\beta$. With the resulting potential, the oscillation of the atoms in the cloud can be numerically simulated and compared to the anharmonic motion observed in the experiment. From this we derive values of $\alpha = 135\,\mathrm{G/cm} \pm 25\,\mathrm{G/cm}$ for the gradient and $\beta = 1.402 \times 10^3 \mathrm{G/cm^2} \pm 4\,\mathrm{G/cm^2}$ for the curvature, leading to the trap frequency $\omega_z = \sqrt{\mu_B \beta_z/m} = 2\pi \times 181.6\,\mathrm{Hz}$. The numerical calculation of the magnetic field configuration confirms the measured gradient [30]. Simple harmonic fits to the oscillation result in the same oscillation frequency with an error better than 10^{-2}. This implies that the effect of the anharmonicity on the atomic motion is less than 1%.

We also analyzed the data by counting the number of atoms in a certain area of momentum space. This area was chosen as a box completely encompassing the diffracted atomic cloud at their highest momentum as indicated by the (red) lines in Fig. 7. The result of this analysis is shown in Fig. 8. Here, the fraction of atoms in the evaluation area relative to the total number of atoms is plotted as a function of time. The peaks are separated by a trap period and represent a revival of the original momentum distribution, directly after the Bragg pulse. For the fit in Fig. 8 (red dashed curve) we assume a Gaussian cloud shape oscillating in and out of the detection volume. The convolution of the Gaussian and the rectangular shape of the detection volume is described by a combination of two error functions with opposite slopes shifted with respect to each other by the time it takes for the cloud to oscillate in and out of the detection volume. The steepness of the slopes is given by the width of the cloud, and this feature is repeated every trap period.

As one can see from Fig. 8(a), the width σ of the cloud's Gaussian momentum distribution broadens with time. If we assume a linear broadening, the fit to the data yields

$$\sigma(t) = \sigma_0 \left(1 + 5 \times 10^{-6} \frac{t}{\mu\mathrm{s}}\right), \tag{16}$$

where σ_0 is the initial width. This broadening is the main reason for the reduction in amplitude and is due to the anharmonicity of the trap. The integrated number of atoms in each peak, on the other hand, decreases much slower. This can be seen in Fig. 8(c), where the integrated number of atoms per peak is plotted against time. In the absence of ^{87}Rb we find a damping time of 3.2 s corresponding to more than 500 oscillations.[1]

[1] In the decompressed trap, we found damping times without ^{87}Rb atoms exceeding 13 s, which is on the order of the magnetic trap lifetime. However, in those traps the presence of a ^{87}Rb cloud has no impact on the ^{6}Li because of gravitational sag.

The exponential decrease of the atom number is due to p-wave collisions between diffracted and undiffracted atoms, since s-wave collisions are forbidden for a spin-polarized Fermi gas. The damping time therefore corresponds to a collision rate of $\gamma_{\mathrm{coll}6p} = 0.3$ Hz. From this the p-wave scattering cross section can be calculated [26, 31]. Here we assume a Gaussian density distribution for the undiffracted atoms and a harmonic oscillation of the diffracted atoms. The relative scattering velocity $v_{\mathrm{sc}} = 2\hbar q/m$ in this system corresponds to a scattering energy of 5 μK × k_{B}. We derive a p-wave scattering cross section of $\sigma_p = 1.4 \times 10^{-13}$ cm^2, which agrees with similar measurements performed on ^{40}K [22] and calculations made for ^{6}Li [32].

In the presence of a cloud of ^{87}Rb, we find a dramatic reduction of the damping time, as can be seen in Figs. 8(b) and (c). The ^{6}Li atoms may collide with ^{87}Rb atoms if these are not initially removed from the trap. The collision time constant calculated from the heteronuclear s-wave scattering length [26] is $\gamma^{-1}_{\mathrm{coll}6,87} = 107$ ms. The exponential damping in the fit of Figs. 8(b) and (c) resulted in a damping time of 113 ms, while the broadening is of the same order as in the case without ^{87}Rb. There is excellent agreement between the calculated collision rate and the observed damping.

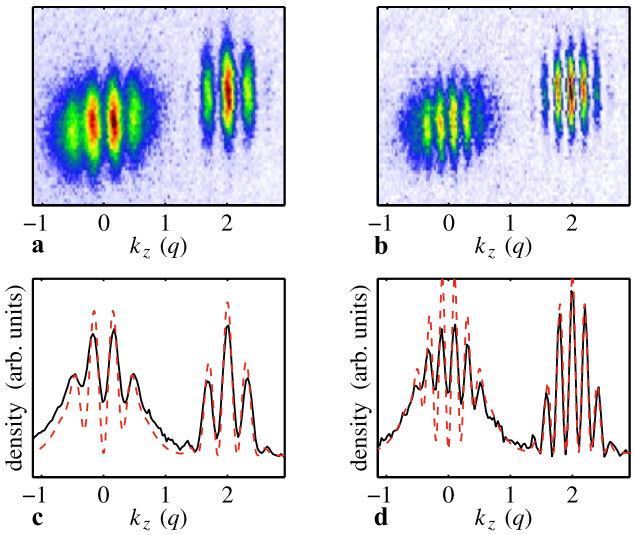

Fig. 9 (**a**, **b**) Absorption images taken after a Ramsey pulse sequence and 2 ms ballistic expansion. (**c**, **d**) Integrations of the absorption images perpendicular to k_z. The (*black*) *solid line* is the experimental data, the (*red*) *dashed line* is a theoretical simulation using (2), (3) and (4). The evolution time between the two Ramsey pulses is $\Delta t = 6$ μs in (**a**, **c**) and $\Delta t = 12$ μs in (**b**, **d**). The temperature used for the simulation is $T = 1.2$ μK and the Rabi frequency is $\Omega_{\mathrm{R}} = 2\pi \times 58$ kHz

5 Atomic coherences

5.1 Ramsey interferometry

The observed revivals of the density distributions after long times indicate that the ^{6}Li atoms are free from any kind of perturbation, which in turn suggests long decoherence times for quantum mechanical superpositions. The existence and the stability of such states can be tested by interferometric experiments.

To this end, we apply a Ramsey sequence of two $\pi/2$-pulses, like in an atomic Mach–Zehnder- (or Ramsey–Bordé-) type interferometer. The beamsplitters are Bragg pulses with a duration equivalent to a pulse area of $\Phi = 0.25$, and the interferometric paths are closed by the kinetic energy released during time-of-flight. We proceed as follows. At time $t = 0$ in the decompressed trap, a first $\pi/2$-pulse of duration τ is applied. Then we wait for a variable amount of time Δt after which a second $\pi/2$-pulse is applied. The momentum distribution is recorded after the delay of half a trap cycle and 2 ms ballistic expansion. Typical time-of-flight absorption images are shown in Figs. 9(a) and (b).

The initial momentum distribution of the atoms gives rise to an inhomogeneous Doppler shift, which detunes the atoms from the Bragg resonance. This allows us to observe all Ramsey fringes in a single shot. We do observe Ramsey fringes for time separations of the Ramsey pulses on the order of up to 30 μs. For longer times, the fringe spacing falls below the resolution limit of the imaging system.

Using (3) the phase difference for the two momentum states of an atom moving at velocity $\hbar k_z/m$ accumulated after a time Δt is given by

$$\phi = \frac{2\hbar(q + k_z)q}{m}\Delta t - \delta. \tag{17}$$

Adjacent fringes are produced by atoms whose velocities differ by an amount $\hbar\Delta k_z/m$ such that $\Delta\phi = 2\pi$, yielding the condition

$$\frac{\hbar\Delta k_z}{m} = \frac{\pi}{q\,\Delta t}. \tag{18}$$

After ballistic expansion during a time t_{tof} the fringes are separated in space by an amount $\pi t_{\mathrm{tof}}/q\,\Delta t$, which must exceed the $\Delta x = 14$ μm resolution of our optical system. From this follows the condition for the maximum allowable Ramsey pulse separation,

$$\Delta t_{\max} = \frac{\pi t_{\mathrm{tof}}}{\Delta x \times q} = 48\ \mu\mathrm{s}. \tag{19}$$

The realistic value is additionally subject to noise.

To a certain extent the contrast can be enhanced by longer TOFs. However this also dilutes the cloud and reduces the quality of the absorption image. Lower temperatures may allow for longer TOFs, but as the temperature of the cloud is

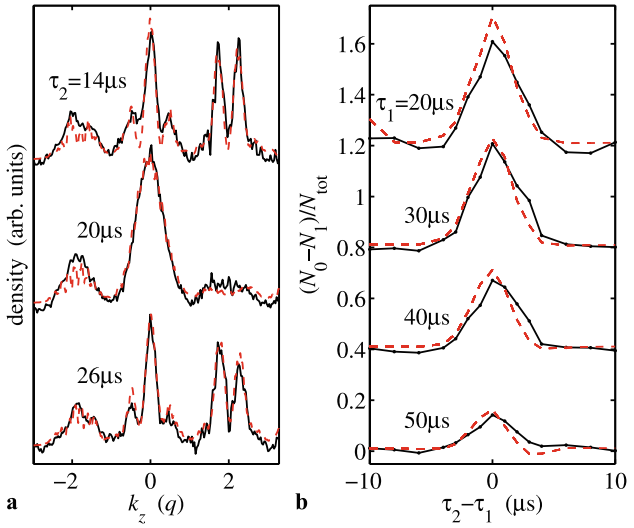

Fig. 10 (**a**) Integrated density of absorption images taken after a spin echo pulse sequence and 2 ms TOF, for a waiting time $\tau_1 = 20$ μs and a variable waiting time τ_2. (**b**) Deviation between the total number of atoms in the zeroth and first exited state. The theoretical curves in *red* (*dashed*) are simulations based on (8), using a Rabi frequency of $\Omega_R = 2\pi \times 220$ kHz

below the Fermi temperature already, the width of the momentum distribution cannot be reduced by much due to the Pauli exclusion principle.

The maximum detectable evolution time could be slightly improved by a better imaging system, however, the general problem remains. It can be circumvented by an echo technique described in the following section.

5.2 Diffraction echo interferometry

Interferometry of particle ensembles is subject to decoherence and dephasing. Decoherence destroys quantum mechanical superpositions due to coupling to a reservoir. In contrast, dephasing results from divergent phase space trajectories for different particles and may be reversed if the trajectories can be inverted [33]. This is possible with echo techniques well known in NMR spectroscopy [23]. They have been successfully applied in cold atom experiments [14] and BEC interferometry [16]. In an echo experiment the free evolution time between two Ramsey pulses is split in two intervals by an additional π-pulse inverting the phase evolution of atomic states. Diffraction echo interferometry is robust against dephasing.

In our case the signature for diffraction echo is the almost complete revival of the zeroth order momentum state. Such an experiment is shown in Fig. 10. It is similar to the Ramsey experiment described above, but the waiting time between the pulses is now divided into two waiting times τ_1 (20 μs in Fig. 10(a)) and τ_2, separated by an additional π-pulse. After completion of a pulse sequence, the atoms are held in the trap for half a trap period, then the trap is turned off and the atoms are imaged after 2 ms ballistic expansion time.

The Rabi frequency in this experiment is $\Omega_R = 2\pi \times 220$ kHz. This ensures Bragg resonance for all atoms according to (10). However, for this Rabi frequency Kapitza–Dirac scattering already occurs, as can be seen in Fig. 10. For times $\tau_2 \neq \tau_1$ the zero-momentum revival is incomplete, it appears as a central peak (dip) in the zeroth (first) order Bragg-diffracted portion. This peak (dip) broadens until for $\tau_2 = \tau_1$ the revival is most pronounced. This effect is also seen in Fig. 10(b), where the difference between atom numbers in the zeroth and first diffracted state is shown.

The revival can be observed for times up to $\tau_{tot} = \tau_1 + \tau_2 = 100$ μs. In a harmonic trapping potential momentum states are no eigenstates, which leads to a mixing of position and momentum coordinates for long evolution times. This process is responsible for the decay of the diffraction echo rather than decoherence. The coherent theoretical model based on (8) fully describes the experimental observation, which leads us to claim τ_{tot} as a lower bound for the coherence time.

Setting the waiting times to a multiple of the oscillation period $\tau_1 = \tau_2 = 2\pi n/\omega_z$ can compensate the effect of the trapping potential as has been shown in [34]. In our experimental setup, revivals of the diffraction echo could not be observed. This might be due to the large momentum spread of the initial cloud.

6 Conclusion

In conclusion, we presented Bragg scattering of fermions from a moving optical lattice. We were able to show the coherence between the zeroth- and first-order diffracted momentum states. Our work presents the first study of interferometry with fermionic atoms using separate interferometric arms and a variable evolution time. The coherence is also observed with a diffraction echo experiment, where a lower bound for the coherence time of $t_{tot} > 100$ μs was found. A longer observation was hampered by the fact that the studied momentum states are no eigenstates of the harmonic trapping potential. The diffracted atoms, however, oscillate in the trapping potential for very long times with a single atom damping time of about 3.2 s. This leads us to the assumption of a similarly long coherence time, which is consistent with the observation made by Roati et al. [20]. Thus fermionic ^{6}Li is a promising candidate for interferometric experiments with long coherence times using schemes similar to [16].

Moreover, we successfully applied Bragg spectroscopy to fermions, measuring the momentum distribution of an ultracold degenerate Fermi gas. Although not deep in the degenerate regime ($T/T_F = 0.6$), the momentum distribution

revealed signs of quantum degeneracy. For even lower temperatures it is conceivable to observe degeneracy from the shape of the distribution directly. In addition, Bragg spectroscopy allows for in-situ probing of specific momentum classes of trapped atoms.

Future work will be devoted to studying a $^{87}Rb + {}^{6}Li$ mixture in a crossed beam dipole trap, using Bragg scattering in the vicinity of one of the recently found heteronuclear Feshbach resonances [35]. Signatures of the interaction energy of the ensemble should be visible in the profile of a Bragg spectrum, similar to the frequency shift observed in Bragg spectroscopy on BECs [1, 2]. Furthermore, Bragg spectroscopy permits to measure the atomic dispersion relation, which is particularly interesting in case of many-body correlations. Bragg spectroscopy should also be applicable to take excitation spectra of fermionic spin mixtures in the BEC-BCS crossover regime which could be realized in our experiment as well.

Acknowledgements During the completion of this paper, we learned that Bragg spectroscopy on fermionic spin mixtures has been done in Tokyo [36] and Melbourne [37]. This work has been supported by the Deutsche Forschungsgemeinschaft (DFG).

References

1. J. Stenger, S. Inouye, A.P. Chikkatur, D.M. Stamper-Kurn, D.E. Pritchard, W. Ketterle, Phys. Rev. Lett. **82**, 4569 (1999)
2. J. Stenger, S. Inouye, D.M. Stamper-Kurn, A.P. Chikkatur, D.E. Pritchard, W. Ketterle, Appl. Phys. B **69**, 347 (1999)
3. M. Kozuma, L. Deng, E.W. Hagley, J. Wen, R. Lutwak, K. Helmerson, S.L. Rolston, W.D. Phillips, Phys. Rev. Lett. **82**, 871 (1999)
4. D.M. Stamper-Kurn, A.P. Chikkatur, A. Görlitz, S. Inouye, S. Gupta, D.E. Pritchard, W. Ketterle, Phys. Rev. Lett. **83**, 2876 (1999)
5. D.M. Stamper-Kurn, W. Ketterle, in *Les Houches 1999 Summer School, Session LXXII* (2000)
6. J. Steinhauer, R. Ozeri, N. Katz, N. Davidson, Phys. Rev. Lett. **88**, 20407 (2002)
7. J. Steinhauer, N. Katz, R. Ozeri, N. Davidson, C. Tozzo, F. Dalfovo, Phys. Rev. Lett. **90**, 060404 (2003)
8. J.R. Abo-Shaeer, D.E. Miller, J.K. Chin, K. Xu, T. Mukaiyama, W. Ketterle, Phys. Rev. Lett. **94**, 040405 (2005)
9. P.B. Blakie, R.J. Ballagh, Phys. Rev. Lett. **86**, 3930 (2001)
10. S.R. Muniz, D.S. Naik, C. Raman, Phys. Rev. A **73**, 041605 (2006)
11. H.P. Büchler, P. Zoller, W. Zwerger, Phys. Rev. Lett. **93**, 080401 (2004)
12. G.M. Bruun, G. Baym, Phys. Rev. A **74**, 033623 (2006)
13. K.J. Challis, R.J. Ballagh, C.W. Gardiner, Phys. Rev. Lett. **98**, 093002 (2007)
14. M. Kasevich, S. Chu, Phys. Rev. Lett. **67**, 181 (1991)
15. J.E. Simsarian, J. Denschlag, M. Edwards, C.W. Clark, L. Deng, E.W. Hagley, K. Helmerson, S.L. Rolston, W.D. Phillips, Phys. Rev. Lett. **85**, 2040 (2000)
16. J.H.T. Burke, B. Deissler, K.J. Hughes, C.A. Sackett, Phys. Rev. A **78**, 023619 (2008)
17. A.P. Chikkatur, A. Görlitz, D.M. Stamper-Kurn, S. Inouye, S. Gupta, W. Ketterle, Phys. Rev. Lett. **85**, 483 (2000)
18. J.M. Vogels, K. Xu, W. Ketterle, Phys. Rev. Lett. **89**, 020401 (2002)
19. S. Inouye, A.P. Chikkatur, D.M. Stamper-Kurn, J. Stenger, D.E. Pritchard, W. Ketterle, Science **285**, 571 (1999)
20. G. Roati, E. de Mirandes, F. Ferlaino, H. Ott, G. Modugno, M. Inguscio, Phys. Rev. Lett. **92**, 230402 (2004)
21. B. DeMarco, D.S. Jin, Phys. Rev. A **58**, R4267 (1998)
22. B. DeMarco, J.L. Bohn, J.P. Burke Jr., M. Holland, D.S. Jin, Phys. Rev. Lett. **82**, 4208 (1999)
23. E.L. Hahn, Phys. Rev. **80**, 580 (1950)
24. F. Riehle, Th. Kisters, A. Witte, J. Helmcke, Ch.J. Bordé, Phys. Rev. Lett. **67**, 177 (1991)
25. C. Marzok, B. Deh, S. Slama, C. Zimmermann, Ph.W. Courteille, Phys. Rev. A **78**, 021602(R) (2008)
26. C. Silber, S. Günther, C. Marzok, B. Deh, Ph.W. Courteille, C. Zimmermann, Phys. Rev. Lett. **95**, 170408 (2005)
27. J. Fortágh, A. Grossmann, T.W. Hänsch, C. Zimmermann, J. Appl. Phys. **84**, 6499 (1998)
28. Z. Li, S. Singh, T. Tscherbul, K.W. Madison, Phys. Rev. A **78**, 022710 (2008)
29. P.B. Blakie, R.J. Ballagh, J. Phys. B, At. Mol. Opt. Phys **33**, 3961 (2000)
30. C. Silber, Dissertation, Eberhard-Karls-Universität Tübingen (2006). http://tobias-lib.ub.uni-tuebingen.de/volltexte/2006/2224/
31. C. Marzok, B. Deh, Ph.W. Courteille, C. Zimmermann, Phys. Rev. A **76**, 052704 (2007)
32. F. Chevy, E.G.M. van Kempen, T. Bourdel, J. Zhang, L. Khaykovich, M. Teichmann, L. Tarruell, S.J.J.M.F. Kokkelmans, C. Salomon, Phys. Rev. A **71**, 062710 (2005)
33. M.F. Andersen, A. Kaplan, N. Davidson, Phys. Rev. Lett. **90**, 023001 (2003)
34. M. Horikoshi, K. Nakagawa, Phys. Rev. Lett. **99**, 180401 (2007)
35. B. Deh, C. Marzok, C. Zimmermann, Ph.W. Courteille, Phys. Rev. A **77**, 010701(R) (2008)
36. Y. Inada, H. Munekazu, S. Nakajiama, M. Kuwata-Gonokami, M. Ueda, T. Mukaiyama, arXiv:0712.1445v4 (2008)
37. G. Veeravalli, E. Kuhnle, P. Dyke, C.J. Vale, arXiv:0809.2145v1 (2008)